

pubs.acs.org/NanoLett Letter

# Ultrathin Ternary FeCoNi Alloy Nanoarrays in BaTiO<sub>3</sub> Matrix for Room-Temperature Multiferroic and Hyperbolic Metamaterial

Jijie Huang,\*,<sup>#</sup> Leigang Li,<sup>#</sup> Zedong Hu, Benson Kunhung Tsai, Jialong Huang, Jianan Shen, Yizhi Zhang, James P. Barnard, Jiawei Song, and Haiyan Wang\*



Cite This: https://doi.org/10.1021/acs.nanolett.4c02036



ACCESS More Article Recommendations Supporting Information

**ABSTRACT:** Multifunctional vertically aligned nanocomposite (VAN) thin films exhibit considerable potential in diverse fields. Here, a BaTiO<sub>3</sub>–FeCoNi alloy (BTO-FCN) system featuring an ultrathin ternary FCN alloy nanopillar array embedded in the BTO matrix has been developed with tailorable nanopillar size and interpillar distance. The magnetic alloy nanopillars combined with a ferroelectric oxide matrix present intriguing multifunctionality and coupling properties. The room-temperature magnetic response proves the soft magnet nature of the BTO-FCN films with magnetic anisotropy has been demonstrated. Furthermore, the anisotropic nature of the dielectric-metal alloy VAN renders it an ideal candidate for hyperbolic metamaterial (HMM), and the epsilon-near-zero (ENZ) wavelength, where the real part of permittivity ( $\varepsilon$ ') turns to negative, can be tailored from ~700 nm to ~1050 nm. Lastly, room-temperature multiferroicity has been demonstrated via interfacial coupling between the magnetic nanopillars and ferroelectric matrix.

KEYWORDS: vertically aligned nanocomposite thin film, soft magnet, hyperbolic metamaterial, multiferroicity

Tertically aligned nanocomposite (VAN) thin films have garnered substantial attention owing to their multifunctionality and strong vertical interfacial coupling, which enable them to exhibit physical properties that are distinct from those found in single-phase materials. 1-4 An illustrative example is the realization of diverse multiferroic thin films through the VAN system design (e.g., combining ferroelectric BaTiO<sub>3</sub> with magnetic CoFe<sub>2</sub>O<sub>4</sub> or SrRuO<sub>3</sub>), 5,6 a property rarely achievable in single-phase materials. Furthermore, in recent years, the selection of materials for VAN thin films has expanded beyond oxides to encompass metals and nitrides, which significantly enhances the design flexibility of VANs, enabling the attainment of extraordinary physical properties that were previously unachievable within oxide—oxide systems. 8-11 To further illustrate, hyperbolic metamaterials have been successfully engineered in several nonoxide-oxide VAN systems, including Au-La<sub>0.67</sub>Sr<sub>0.33</sub>MnO<sub>3</sub>, <sup>12</sup> NiO-TiN, <sup>9</sup> Cu-ZnO, 13 and others. Notably, the performance of these metamaterials can be further fine-tuned through the implementation of three-dimensional VAN designs, which

involves the incorporation of VAN and multilayer structures and provides additional avenues for tailoring the properties and functionalities of these metamaterials to meet specific application requirements. What is even more intriguing is that conventional two-phase VANs have evolved into multiphase systems by integrating multiple metals with oxides or nitrides, which not only opens up new avenues for designing multifunctional VANs but also serves as a valuable platform for investigating the interfacial coupling between different categories of materials. <sup>16–18</sup>

On another front, magnetic nanopillar arrays (MNA) hold significant promise in various applications, including magnetic

Received: April 29, 2024 Revised: August 1, 2024 Accepted: August 1, 2024



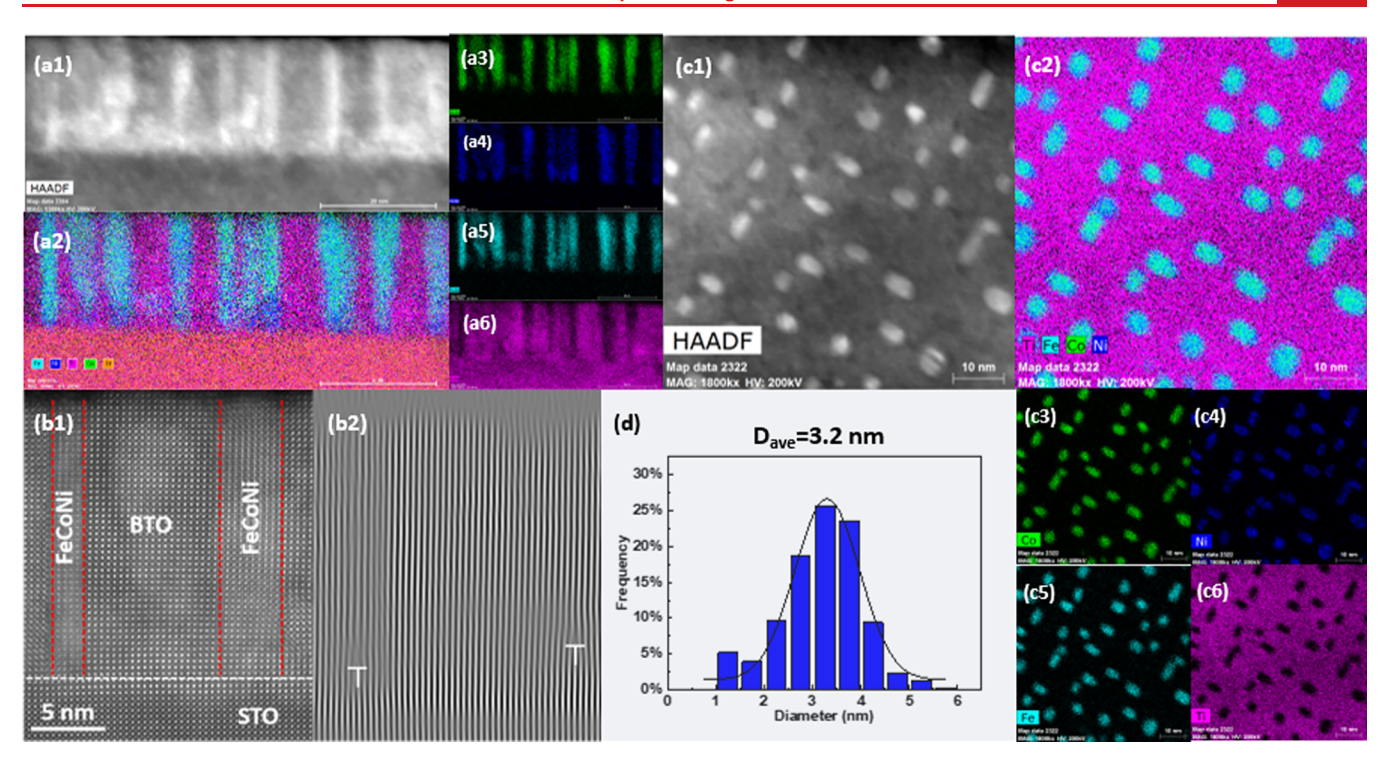


Figure 1. Detailed microstructure characterization of the BTO-FCN film deposited at 5 Hz. (a1) Low-mag cross-sectional STEM image with corresponding (a2) EDS mapping of (a3) Co, (a4) Ni, (a5) Fe, and (a6) Ti elements; (b1) high-resolution cross-sectional HAADF STEM image with corresponding (b2) masked inverse FFT image; (c1) low-mag plan-view STEM image with corresponding (c2) EDS mappings of (c3) Co, (c4) Ni, (c5) Fe, and (c6) Ti elements; (d) distribution of the nanopillar diameter based on the plan-view image.

data storage devices, 19 magnetic field and acoustic sensors, 20 and high-frequency microwave electronics,<sup>21</sup> and others. The predominant method employed for synthesizing MNA involves porous alumina template electrodeposition, and the dimensions of the nanopillars are closely linked to the diameter of the pores, which typically exceed 10 nm in size.<sup>22</sup> Remarkably, it has been observed that ultrathin (less than 5 nm) MNA can be synthesized through the design of magnetic metal-oxide VANs, which holds great promise, particularly in the area of highdensity magnetic data storage applications.<sup>23</sup> While several MNAs composed of commonly used magnetic metals, such as Fe, Co, and Ni, have been realized within the framework of metal-oxide VANs, 10,16,24,25 it is worth noting that a ternary FeCoNi (FCN) alloy-based MNA embedded within a VAN structure has yet to be developed. Ternary FCN alloy MNAs have garnered significant attention due to their exceptional magnetically soft properties, rendering them ideal candidates for use in electromechanical devices and other applications.<sup>26</sup>

In this work, we have successfully fabricated a VAN structure comprising a ternary  $F_{1/3}C_{1/3}N_{1/3}$  MNA embedded within a BaTiO<sub>3</sub> (BTO) matrix, denoted as BTO-FCN, utilizing the pulsed laser deposition (PLD) technique. To precisely tailor the size of the FCN nanopillars and thereby modulate the magnetic anisotropy (especially shape anisotropy) of the MNA, we exercised control over the laser frequency during deposition. Furthermore, the selection of the ferroelectric BTO matrix provides the possibility to obtain a multiferroic nanocomposite thin film, which contains both the ferromagnetic FCN and ferroelectric BTO phases. To this end, a BTO/BTO-FCN bilayer structure has been developed, which has enabled the realization of multiferroicity. This advancement not only underscores the significance of the BTO-FCN system but also serves as a platform for achieving multiferroicity

within metal-oxide VANs, opening up new avenues for multifunctional materials.

First, standard  $\theta$ -2 $\theta$  X-ray diffraction (XRD) patterns of the BTO-FCN deposited at varied frequencies have been measured and plotted in Figure S1, BTO (00l) peaks were identified, while no obvious FCN peaks existed, which might be due to the ultrasmall size of the nanopillars. It is worth noting that minor additional peaks of BTO (111) and BTO (220) were identified in some of the films, which could be attributed to the relatively large lattice mismatch of 12% between BTO (4.031 Å) and FCN (3.573 Å). The main portion of the BTO phase grows along the (00l) orientation, and the nanocomposite films follow the typical VAN structure growth, evidenced by the high-resolution STEM images provided in Figure S2. The minor misoriented domains might not affect the main physical properties of the films. Subsequently, the surface morphology of the films was characterized by atomic force microscopy (AFM), as shown in Figure S3a-3e with the 1 Hz, 2 Hz, 5 Hz, 10 Hz, and 20 Hz deposited films. All the films exhibit a smooth surface with a root-mean-square (RMS) surface roughness of less than 0.560 nm, indicative of high film quality. Interestingly, the RMS values demonstrate a diminishing trend with increasing deposition frequency (shown in Figure S3f), which is likely attributed to the increased deposition rate associated with higher frequencies. Then, scanning transmission electron microscopy (STEM) imaging, encompassing both crosssectional and plan views, was employed to elucidate the three-dimensional structure of the BTO-FCN films. In Figure 1a1, a low-magnification cross-sectional STEM image of the 5 Hz sample is depicted, accompanied by corresponding energydispersive X-ray spectroscopy (EDS) images displayed in Figure 1a2-a6. The thickness of the film is estimated to be

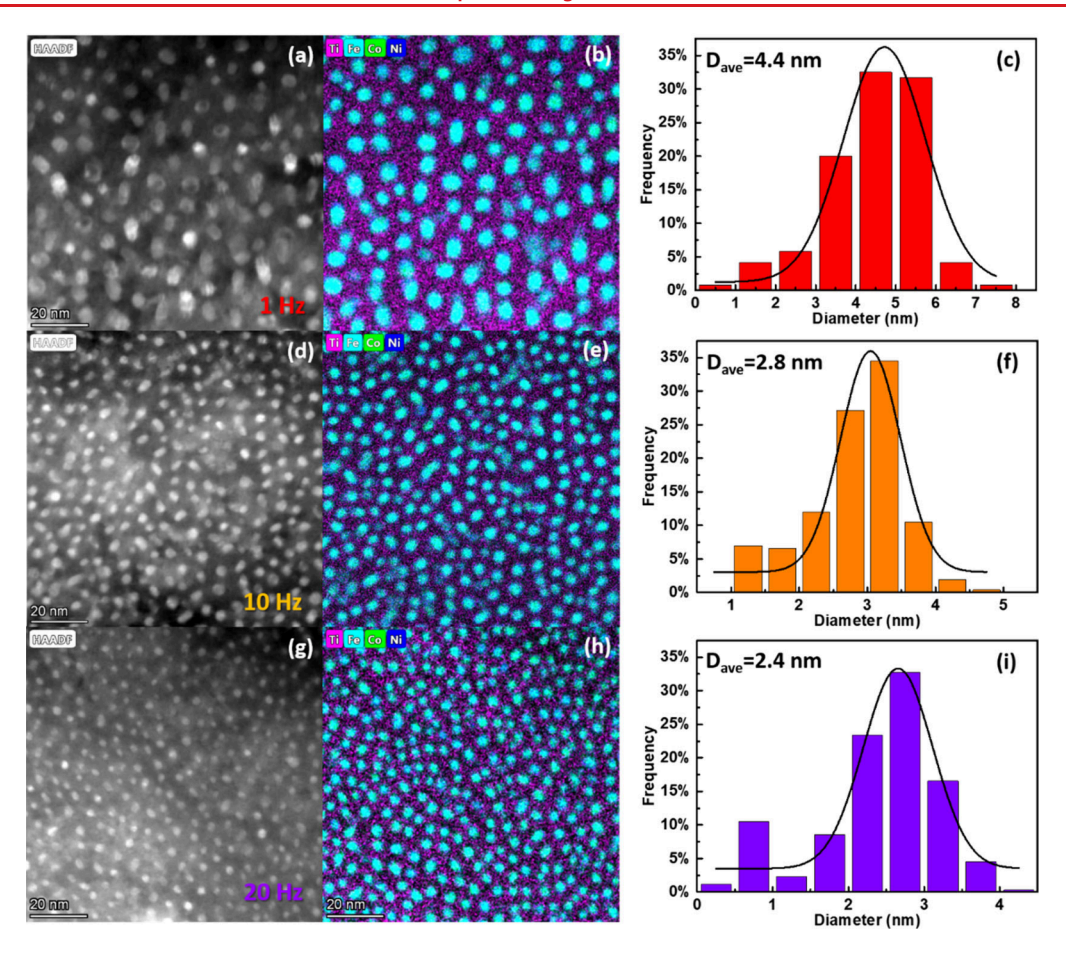


Figure 2. Structure comparison of the BTO-FCN films deposited at different laser frequencies. Low-mag STEM, EDS mapping, and FeCoNi alloy nanopillar diameter distribution of the (a-c) 1 Hz, (d-f) 10 Hz, and (g-(i) 20 Hz deposited films.

~20 nm. The presence of Fe, Co, and Ni elements within the nanopillars suggests the formation of an FCN alloy nanoarray embedded within the BTO matrix. Further characterization utilizing high-angle annular dark field (HAADF) STEM imaging, as illustrated in Figure 1b1, unveils the high crystallinity or nearly epitaxial growth of the film at the atomic scale, which could be further demonstrated in the STEM images (Figure S2) showing multiple regions with the epitaxial growth of the film. Notably, distinct lattice arrangements are observed for both the BTO and the ternary FCN alloy phases. Very limited defects (e.g., dislocations) are observed at the interface area, as evidenced by the masked inverse fast Fourier transform (FFT) image in Figure 1b2, further indicating the high quality of the nanocomposite film. The low-magnification plan-view image in Figure 1c1, along with corresponding EDS mappings in Figure 1c2-c6, offer a horizontal perspective, therefore, an overall alloy nanoarray-in-matrix structure could be determined. Based on the plan-view image, the distribution of nanopillar diameters was plotted in Figure 1d, yielding an estimated average diameter ( $D_{ave}$ ) of 3.2 nm.

To facilitate a comparative analysis of the BTO-FCN structures fabricated at different laser frequencies, plan-view STEM images (Figure 2a,d,g) alongside the corresponding EDS mappings (Figure 2b,e,h) were obtained for the 1 Hz, 10 Hz, and 20 Hz deposited films. A consistent FCN alloy nanoarray-in-matrix structure is identified with varying nanopillar size, and the  $D_{ave}$  of the nanopillars is estimated to be 4.4 nm, 2.8 nm, and 2.4 nm, respectively, as estimated from the distribution plots in Figure 2c,f,i. Similar characterizations of

the 2 Hz sample are provided in Figure S4, with a calculated  $D_{ave}$  value of 3.5 nm. Consequently, a discernible trend of decreasing  $D_{ave}$  of FCN nanopillars with increasing laser frequency was determined (as shown in Figure S5), aligning with previous findings on the BaZrO<sub>3</sub>–Co system. <sup>23</sup> Of particular interest, the 20 Hz deposited film presented the smallest nanopillars of  $D_{ave}$  = 2.4 nm and the highest nanopillar density of 2 × 10<sup>13</sup>/inch<sup>2</sup>. Such ultrasmall MNA structures hold promise as ideal candidates for a perpendicular magnetic recording (PMR) device, where each FCN nanopillar corresponds to one bit. Thus, the high nanopillar density in the 20 Hz deposited film translates to a substantial storage capacity of 2.3 Tb/inch<sup>2</sup>. Overall, the BTO-FCN system yields a well-defined MNA-in-matrix configuration with nanopillar size and density easily tunable through deposition frequency modulation.

The development of the ternary FCN alloy MNA via the one-step self-assembled approach offers great advantages, particularly in achieving ultrathin structure and tunable size. The magnetic properties of the FCN alloy MNAs with varying nanopillar size have been characterized and compared, as shown in Figure 3a—e with the room-temperature (RT) magnetic hysteresis (MH) loops (applied field perpendicular (OP) or parallel (IP) to the film surface) for the films deposited at 1 Hz, 2 Hz, 5 Hz, 10 Hz, and 20 Hz, respectively. The coercivity ( $H_C$ ) of all the samples is compared in Figure 3f; the 1 Hz film exhibits the highest  $H_{C-OP}$  and  $H_{C-IP}$  of ~800 Oe and ~110 Oe, respectively. Interestingly, all the other samples display soft magnetic behavior with low  $H_{C-OP}$  and

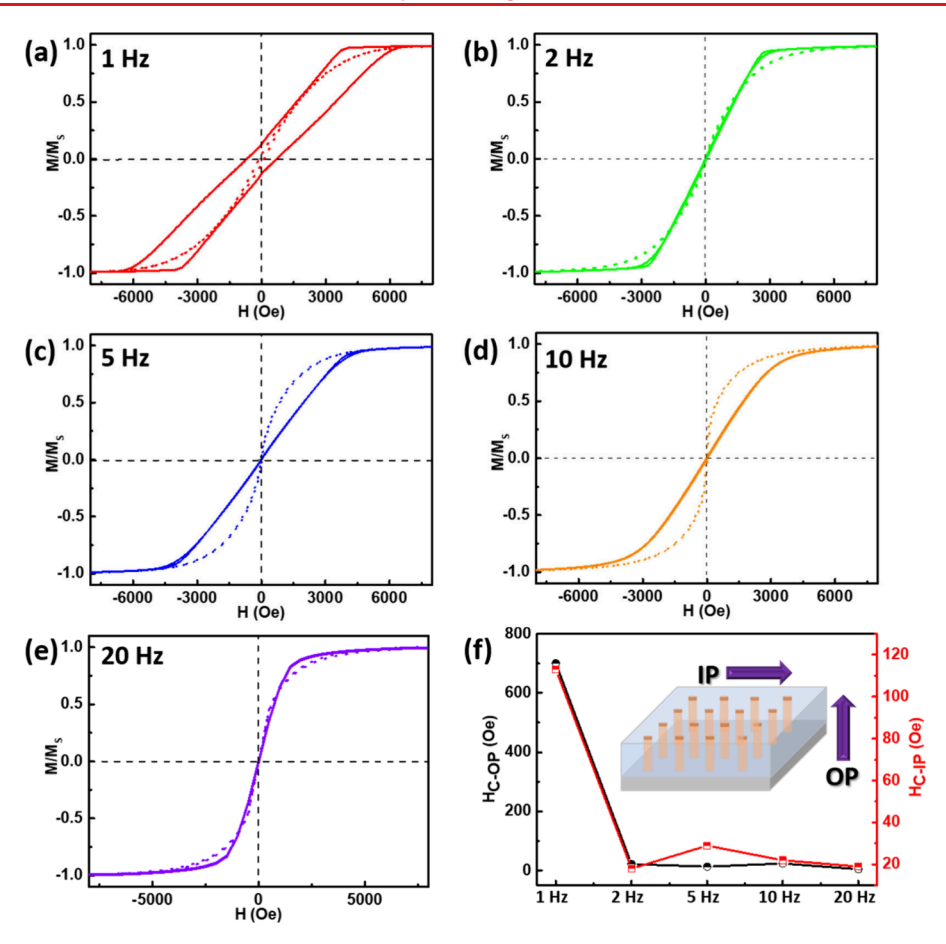


Figure 3. Room-temperature magnetic hysteresis loops of the samples deposited at (a) 1 Hz, (b) 2 Hz, (c) 5 Hz, (d) 10 Hz, and (e) 20 Hz; the solid and dashed lines present the applied field perpendicular (OP) and parallel (IP) to the film surface, respectively; (f) OP and IP coercivity comparison of the films deposited at different frequencies.

 $H_{C-IP}$  values (less than 20 Oe), which is lower than the FCN MNAs fabricated by templated electrodeposition, 27,28 indicating their great potential in soft magnet applications. The higher  $H_c$  value observed in the 1 Hz sample is attributed to the larger size of the alloy nanopillars within this film compared to those in other samples. There exists a critical radius  $R_c$  to define the magnetic reversal modes as either the curling or the coherent rotation mode,29 which could be expressed as  $R_{c}=\sqrt{kA/\mu_{0}M_{S}^{\ 2}};$  here, k is a constant (1.08 for an infinite cylinder); A is the exchange stiffness constant  $(1.0 \times 10^{-6} \text{ erg})$ cm<sup>-1</sup> for the FeCoNi alloy; here, the average value of Fe, Co, and Ni bulk was adopted);  $M_S$  is the saturation magnetization for the FeCoNi alloy (1.6  $\times$  10<sup>6</sup> A m<sup>-1</sup>), which results in  $R_c$  = 1.83 nm and diameter  $d_c = 3.66$  nm. As we can see,  $d_{1 Hz} > d_c$ follows the curling mode, whereas all of the others adhere to the coherent rotation mode. Typically, the  $H_C$  value varies very little when the diameter of the nanopillars is smaller than the critical diameter, therefore, all the films except the 1 Hz sample exhibit similar  $H_C$  values. Furthermore, the interpillar distance in the higher frequency deposited films is smaller, leading to magnetostatic interaction between nearby nanopillars, which contributes to the lower  $H_C$  values.<sup>30</sup> Another feature of the MNAs is magnetic anisotropy, elucidated through disparate OP and IP MH curves. In FCN MNAs, the magnetic anisotropy arises from three factors: (i) shape anisotropy; (ii) interpillar magnetostatic dipole interaction; and (iii) magnetocrystalline anisotropy, contributing to the total

effective anisotropy field  $H_K = 2\pi M_S - 6.3\pi M_S r^2 L d^{-3} +$  $H_{\rm MC}$ . Here,  $M_{\rm S}$  is the saturation magnetization, L and r are the length and radius of the nanopillars, and d is the interpillar distance. Previous studies suggest negligible magnetocrystalline anisotropy in FCN nanopillars.<sup>32</sup> In this case, the  $H_K$  values of all the films are negative, suggesting the interpillar magnetostatic dipole interaction is the dominate factor, with the easy magnetization axis perpendicular to the nanopillars' long axis (or parallel to the film surface). 27,33 It is noted that the thickness of the films was kept the same, ~20 nm. Tuning the thickness of the films could change their magnetic anisotropy. For example, shape anisotropy could dominate in thick films (i.e., long nanopillars). The MH loops of all the films measured at 10 K are shown in Figure S6, where magnetic anisotropy is also discerned from variations in the shapes of the OP and IP curves. Then, the 5 Hz sample was selected for the MH measurements at varying temperatures, as shown in Figure S7. The H<sub>C</sub> value decreases with increasing temperature, which indicates the thermally activated magnetization reversal process.

On the other hand, the structure of FCN MNAs with ultrathin nanopillars (significantly smaller than effective wavelength) in the BTO matrix serves well as one of the two typical hyperbolic metamaterial (HMM) structures, which extends the BTO-FCN system for applications as optical sensors. Angular-dependent ellipsometry measurements were conducted to verify the potential HMM, with the uniaxial model applied to fit the optical complex dielectric functions

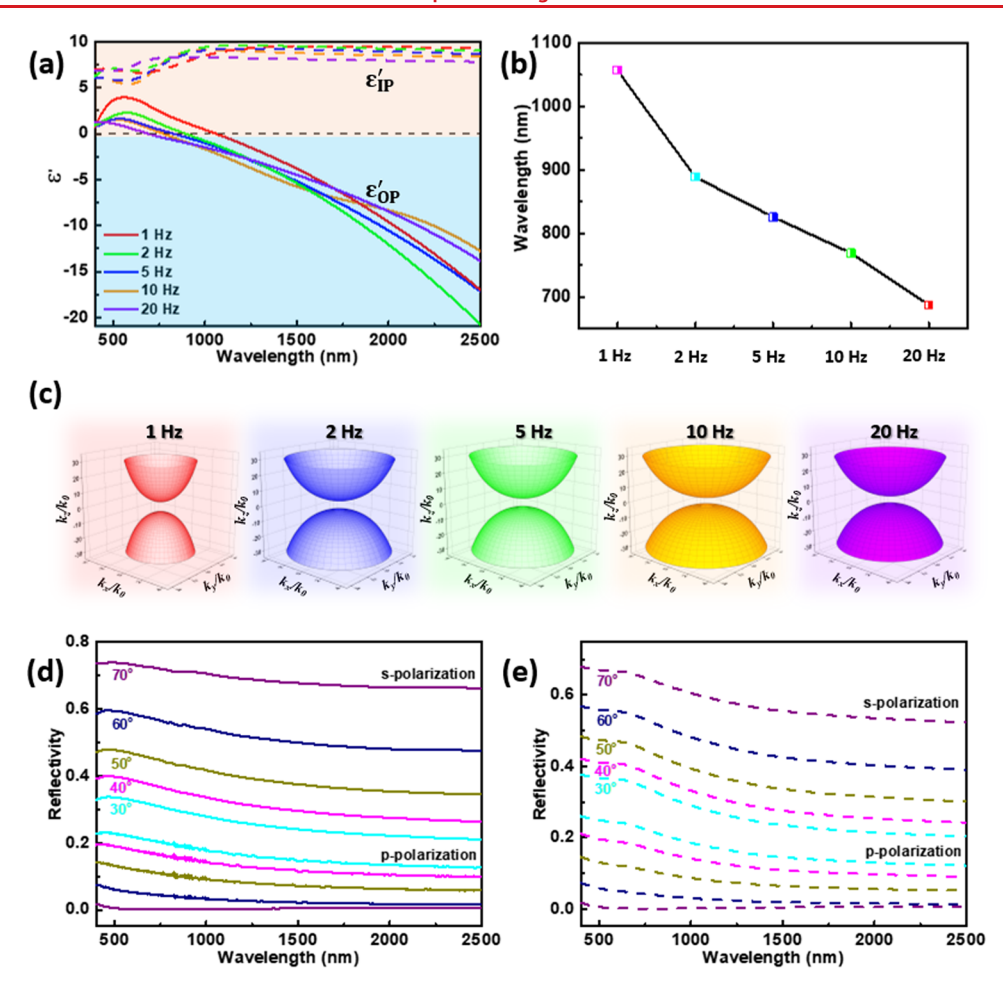


Figure 4. Optical properties of the BTO-FCN thin films. (a) Real part of the complex dielectric function ( $\varepsilon'$ ) of the BTO-FCN films in OP (perpendicular to film surface) and IP (parallel to film surface) directions; (b) comparison of the wavelength of  $\varepsilon'$  starts to be negative of the films deposited at different laser frequencies; (c) the extracted isofrequency surfaces at 1200 nm of all the samples; (d) experimental and (e) simulated reflectivity spectra of the 20 Hz sample at different angles of incidence for p-polarized and s-polarized incident light.

(real part  $\varepsilon'$  and imaginary part  $\varepsilon''$ ) in both the OP and IP directions, as shown in Figure 4a for  $\varepsilon'$  and Figure S8 for  $\varepsilon''$ , respectively. As seen, the  $arepsilon_{IP}$  maintains positive value throughout the entire fitted wavelength of 400 to 2500 nm, while  $\varepsilon_{OP}$  starts to be negative at a specific wavelength for all the VAN films, indicative of transverse-positive dispersion. Notably, there is a blue shift in the epsilon-near-zero (ENZ) wavelength with increasing deposition frequency, ranging from approximately 700 nm for the 20 Hz sample to around 1050 nm for the 1 Hz film (Figure 4b). The shift of the ENZ wavelength is mainly caused by the varying nanopillar distribution, or more exactly, the filling ratio of the metal alloy nanopillars. In a metal nanopillars-in-dielectric system, the dynamical Maxwell-Garnett theory could be employed to determine the permittivity of  $\varepsilon_{OP} = p\varepsilon_m + (1 - p)\varepsilon_d$  and  $\varepsilon_{IP}' = \varepsilon_d + \frac{p\varepsilon_d(\varepsilon_m - \varepsilon_d)}{\varepsilon_d + (1 - p)(\varepsilon_m - \varepsilon_d)q_{eff}};$  here, p is the filling ratio of the metal nanopillars;  $\varepsilon_m$  and  $\varepsilon_d$  represent the permittivity of the metal and dielectric, respectively;  $q_{eff}$  is the effective depolarization factor perpendicular to nanopillars. Therefore, as the permittivity of metal and dielectric is the same for the system, the filling ratio p determines the negative  $\varepsilon_{OP}$ . From the plan-view STEM images, the filling ratio of the alloy nanopillars increases with increasing deposition frequency, leading to the blue shift of the ENZ wavelength, which is

consistent with the previous reports on Ag36 and Au37 nanowires in oxides. Furthermore, the electromagnetic wave (k-wavevector) of such uniaxial anisotropic BTO-FCN films could be manifested by the dispersion relation:  $\frac{k_x^2 + k_y^2}{\epsilon_1} + \frac{k_z^2}{\epsilon_{\parallel}} = \frac{\omega^2}{c^2} = k_0^2 \omega, \text{ where } k_x, k_y, \text{ and } k_z \text{ are the}$ wavevector components in the [100], [010], and [001] directions, respectively;  $\omega$  and c are the frequency and speed of light, respectively. To compare, isofrequency k-space surfaces at 1200 nm for all the films have been plotted in Figure 4c, revealing that all the films belong to class one hyperbolic metamaterial with a hyperbola with two sheets being obtained. The geometry of the isofrequency k-space surfaces varies among different films, indicating the tailorable optical property of the nanocomposite thin film via simply tuning the growth parameter. Optical anisotropy can be further demonstrated by angular-dependent and polarization-resolved reflectivity measurement with the incident angles at 30°, 40°, 50°, 60°, and 70°, as shown in Figure 4d,e with the measured and simulated results of the 20 Hz sample. It is noteworthy that reflectivity increases with rising incident angle when spolarized light strikes the film surface, in accordance with classical electromagnetic theory.<sup>38</sup> However, the opposite trend is observed with p-polarized light incidence, leading to an overall reduction in reflectivity compared with s-polarized

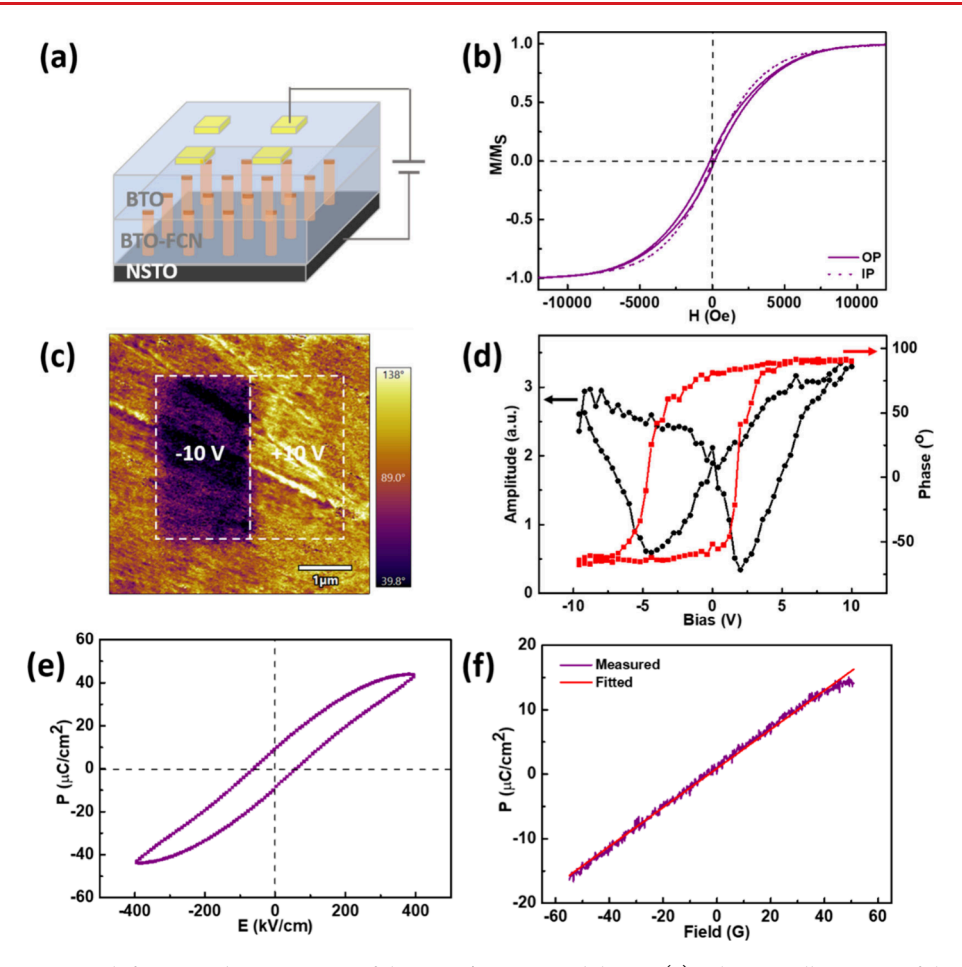


Figure 5. Room-temperature multiferroicity demonstration of the BTO/BTO-FCN bilayers. (a) Schematic illustration of the bilayer film; (b) MH curves in both the OP and IP field measured at room temperature; (c) phase switching map; (d) butterfly-like displacement-voltage (*D-V*) loop and the hysteresis phase-voltage loop; (e) *P-E* loop; (f) magnetoelectric (ME) coupling measurement.

light at the same incident angle. The experimental and simulated angular-dependent and polarization-resolved reflectivity of all the other films are shown in Figure S9, demonstrating similar optical anisotropic characteristics.

Lastly, we demonstrate the multiferroicity of the VAN system by combining ferroelectric BTO and magnetic FCN phases; however, the conducting alloy nanopillar throughout the entire film thickness impedes the employment of the external electrical field. Therefore, an additional BTO layer was deposited atop the BTO-FCN layer to demonstrate the multiferroic composite thin film, and a Nb-STO substrate was used as the bottom electrode, as schematically illustrated in Figure 5a. As a result, two BTO peaks from the BTO-FCN layer and top BTO layer could be identified in the XRD pattern in Figure S10. The MH curves in both the OP and IP directions were measured at room temperature and plotted in Figure 5b, confirming the soft magnetic response. To investigate the ferroelectric property, piezoelectric force microscopy (PFM) was conducted. By applying DC biases of -10 V and +10 V, two neighboring 1.5  $\mu\text{m}^*3$   $\mu\text{m}$  domains were written, resulting in observed out-of-plane domain switching. This is evident from the distinct color contrast in the phase and amplitude switching maps in Figures 5c and S11, respectively. The butterfly-like displacement-voltage (D-V) loop and the hysteresis phase-voltage loop with a sharp 180° change in Figure 5d further confirm the local ferroelectricity in the film. Additionally, a polarization-electric field (P-E) loop

was measured to explore the ferroelectricity on a macroscale (shown in Figure 5e), which exhibits apparent ferroelectricity with a saturation polarization  $(P_s)$  of 45  $\mu$ C/cm<sup>2</sup>, remnant polarization  $(P_r)$  of 9.5  $\mu$ C/cm<sup>2</sup>, and coercive field  $(E_c)$  of ~60 kV/cm. The ferroelectric property results from both the top BTO layer and the BTO in the BTO-FCN layer, and the conducting metal alloy nanopillars in the nanocomposite layer lead to the relatively imperfect ferroelectricity in the film. Furthermore, as the BTO-FCN films were deposited under vacuum conditions, oxygen vacancies might exist in the BTO matrix, which might lead to increased leakage current and deteriorate the ferroelectric property. This could also be one of the reasons for the relatively weak ferroelectricity in the nanocomposite thin films. In addition, strain could be induced in the BTO phase, due to the lattice mismatch and smaller elastic modulus of BTO (67 GPa) compared to the FCN phase (175 GPa), which could also influence the ferroelectric property. Finally, magnetoelectric (ME) coupling measurement was conducted to demonstrate the room-temperature multiferroicity, as indicated by the purple line in Figure 5f. The ME charge coefficient  $\alpha$  was determined to be 0.3022  $\mu$ C/cm<sup>2</sup> Oe from the red linear fitting line. The ME voltage coefficient  $\alpha_{\rm ME}$  could then be calculated through  $\alpha = \alpha_{\rm ME} \varepsilon_0 \varepsilon_r$ ; here,  $\varepsilon_0$  and  $\varepsilon_r$  are the vacuum and relative permittivity of the sample, in this case, the room temperature  $\varepsilon_r$  of an epitaxial BTO thin film. Consequently, the  $\alpha_{ME}$  value was calculated to be 6823 V/cm·Oe, which is larger than previously reported BTO-based

nanocomposite thin film, <sup>40</sup> superlattice, <sup>41</sup> and bulk composite, <sup>42</sup> indicating the strong room-temperature ME coupling of this system. The ME coupling effect, especially the ferroelectric property, could be further improved through growth condition optimization as well as film structure design.

The successful fabrication of an oxide-alloy VAN further expands the material selection for nanocomposite thin film design with tailored functionalities for diverse applications. Future efforts could be focusing on the precise control over the architecture of the oxide-alloy VANs, i.e., the uniform distribution of the nanopillars in the film, which stands as a pivotal challenge in the field of VANs. Moreover, a deeper understanding of the growth mechanisms underlying different nanocomposite thin film systems is essential, as various nanostructures were obtained such as the typical nanopillarin-matrix, 12 core-shell nanopillar-in-matrix, 13 and nanoparticle-in-matrix, 43 in addition to the emergence of new phases. 44 Lastly, leveraging the multifunctionality inherent in oxide-alloy VANs, particularly exemplified by the BTO-FCN system, holds immense potential for integrating multiple functionalities into a single device platform. By exploitation of the synergistic interactions between the oxide and alloy components, novel device architectures with enhanced performance characteristics can be envisioned, paving the way for transformative advancements in various technological domains.

In summary, BTO-FCN nanocomposite thin films with an alloy nanoarray-in-matrix structure have been demonstrated with tunable nanopillar size and interpillar distance. The oxidealloy VANs exhibit interesting physical properties, such as a room-temperature soft magnetic response with coercivity less than 20 Oe, anisotropic magnetic and optical performance, as well as class one hyperbolic metamaterial behavior. Furthermore, the BTO/BTO-FCN bilayer was fabricated to realize the room-temperature multiferroicity, pronounced ferroelectricity with a saturation polarization ( $P_s$ ) of 45  $\mu$ C/cm<sup>2</sup>, remnant polarization  $(P_r)$  of 9.5  $\mu$ C/cm<sup>2</sup>, and coercive field  $(E_c)$  of ~60 kV/cm were achieved, along with an ME voltage coefficient  $\alpha_{\rm ME}$  of 6823 V/cm·Oe. The findings suggest that metamaterials utilizing BTO-alloy VANs offer a promising avenue for the development of multifunctional devices, which opens up opportunities for their integration into various device architectures, enabling the synergistic coupling of these diverse functionalities.

#### ASSOCIATED CONTENT

#### Supporting Information

The Supporting Information is available free of charge at https://pubs.acs.org/doi/10.1021/acs.nanolett.4c02036.

θ-2θ XRD scans, HAADF STEM images, AFM images, magnetic hysteresis loops measured at 10 K, imaginary part of complex dielectric function, experimental and simulated reflectivity spectra of the BTO-FCN films; XRD pattern and amplitude switching map of BTO/BTO-FCN bilayer (PDF)

#### AUTHOR INFORMATION

### **Corresponding Authors**

Jijie Huang — School of Materials, Shenzhen Campus of Sun Yat-sen University, Shenzhen 518107, China; School of Materials Engineering, Purdue University, West Lafayette, Indiana 47907, United States; orcid.org/0000-0002-0858-6670; Email: huangjj83@mail.sysu.edu.cn Haiyan Wang — School of Materials Engineering, Purdue University, West Lafayette, Indiana 47907, United States; School of Electrical and Computer Engineering, Purdue University, West Lafayette, Indiana 47907, United States; orcid.org/0000-0002-7397-1209; Email: hwang00@purdue.edu

#### **Authors**

Leigang Li — College of Materials Science and Engineering,
 Ocean University of China, Qingdao 266100, China
 Zedong Hu — School of Electrical and Computer Engineering,
 Purdue University, West Lafayette, Indiana 47907, United
 States

Benson Kunhung Tsai – School of Materials Engineering, Purdue University, West Lafayette, Indiana 47907, United States

Jialong Huang — School of Materials Engineering, Purdue University, West Lafayette, Indiana 47907, United States Jianan Shen — School of Materials Engineering, Purdue University, West Lafayette, Indiana 47907, United States; orcid.org/0000-0003-3226-2761

Yizhi Zhang — School of Materials Engineering, Purdue University, West Lafayette, Indiana 47907, United States James P. Barnard — School of Materials Engineering, Purdue University, West Lafayette, Indiana 47907, United States; orcid.org/0000-0002-7570-952X

Jiawei Song — School of Materials Engineering, Purdue University, West Lafayette, Indiana 47907, United States

Complete contact information is available at: https://pubs.acs.org/10.1021/acs.nanolett.4c02036

#### **Author Contributions**

<sup>#</sup>Jijie Huang and Leigang Li contributed equally to this work.

Notes

The authors declare no competing financial interest.

#### ACKNOWLEDGMENTS

This study was in part supported by Shenzhen Science and Technology Program (JCYJ20210324133610028) and Guangdong Basic and Applied Basic Research Foundation (2023A1515012594). The work conducted at Purdue University was supported by the U.S. National Science Foundation (DMREF-2323752 for film growth and property characterizations, and DMR-2016453 for HRTEM characterization).

## **■** REFERENCES

- (1) Huang, J.; MacManus-Driscoll, J. L.; Wang, H. New Epitaxy Paradigm in Epitaxial Self-assembled Oxide Vertically Aligned Nanocomposite Thin Films. *J. Mater. Res.* **2017**, 32 (21), 4054–4066.
- (2) MacManus-Driscoll, J. L. Self-assembled Heteroepitaxial Oxide Nanocomposite Thin Film Structures: Designing Interface-induced Functionality in Electronic Materials. *Adv. Funct. Mater.* **2010**, 20, 2035–2045.
- (3) Huang, J.; Li, W.; Yang, H.; MacManus-Driscoll, J. L. Tailoring Physical Functionalities of Complex Oxides by Vertically Aligned Nanocomposite Thin-film Design. *MRS Bull.* **2021**, *46*, 159–167.
- (4) Wang, G.; Sun, F.; Zhou, S.; Zhang, Y.; Zhang, F.; Wang, H.; Huang, J.; Zheng, Y. Enhanced Memristive Performance via a Vertically Heterointerface in Nanocomposite Thin Films for Artificial Synapses. ACS Appl. Mater. Interfaces 2024, 16, 12073–12084.
- (5) Zheng, H.; Wang, J.; Lofland, S. E.; Ma, Z.; Mohaddes-Ardabili, L.; Zhao, T.; Salamanca-Riba, L.; Shinde, S. R.; Ogale, S. B.; Bai, F.; Viehland, D.; Jia, Y.; Schlom, D. G.; Wuttig, M.; Roytburd, A.;

- Ramesh, R. Multiferroic  $BaTiO_3$ - $CoFe_2O_4$  Nanostructures. *Science* **2004**, 303 (5658), 661–663.
- (6) Wang, F.; Jiang, C.; Huang, J. Multiferroic Thin Film via SrRuO<sub>3</sub>-BaTiO<sub>3</sub> Vertically Aligned Nanocomposite Design. *Appl. Phys. Lett.* **2020**, *117*, 162902.
- (7) Kuo, C.; Hu, Z.; Yang, J.; Liao, S.; Huang, Y.; Vasudevan, R.; Okatan, M.; Jesse, S.; Kalinin, S.; Li, L.; Liu, H.; Lai, C.; Pi, T.; Agrestini, S.; Chen, K.; Ohresser, P.; Tanaka, A.; Tjeng, L.; Chu, Y. Single-domain Multiferroic BiFeO<sub>3</sub> Films. *Nat. Commun.* **2016**, *7*, 12712.
- (8) Misra, S.; Wang, H. Review on the Growth, Properties and Applications of Self-assembled Oxide-metal Vertically Aligned Nanocomposite Thin Films-Current and Future Perspectives. *Mater. Horiz.* **2021**, *8* (3), 869–884.
- (9) Wang, X.; Wang, H.; Jian, J.; Rutherford, B.; Gao, X.; Xu, X.; Zhang, X.; Wang, H. Metal-free Oxide-nitride Heterostructure as a Tunable Hyperbolic Metamaterial Platform. *Nano Lett.* **2020**, *20* (9), 6614–6622.
- (10) Weng, X.; Hennes, M.; Juhin, A.; Sainctavit, P.; Gobaut, B.; Otero, E.; Choueikani, F.; Ohresser, P.; Tran, T.; Hrabovsky, D.; Demaille, D.; Zheng, Y.; Vidal, F. Strain-engineering of Magnetic Anisotropy in Co<sub>x</sub>Ni<sub>1-x</sub>-SrTiO<sub>3</sub>/SrTiO<sub>3</sub> (001) Vertically Assembled Nanocomposites. *Phys. Rev. Materials* **2022**, *6*, 046001.
- (11) Huang, J.; Wang, X.; Hogan, N.; Wu, S.; Lu, P.; Fan, Z.; Dai, Y.; Zeng, B.; Starko-Bowes, R.; Jian, J.; Wang, H.; Li, L.; Prasankumar, R.; Yarotski, D.; Sheldon, M.; Chen, H.; Jacob, Z.; Zhang, X.; Wang, H. Nanoscale Artificial Plasmonic Lattice in Self-assembled Vertically Aligned Nitride-metal Hybrid Metamaterials. *Adv. Sci.* **2018**, *5* (7), 1800416.
- (12) Huang, J.; Wang, H.; Qi, Z.; Lu, P.; Zhang, D.; Zhang, B.; He, Z.; Wang, H. Multifunctional Metal-oxide Nanocomposite Thin Film with Plasmonic Au Nanopillars Embedded in Magnetic La<sub>0.67</sub>Sr<sub>0.33</sub>MnO<sub>3</sub> Matrix. *Nano Lett.* **2021**, *21*, 1032–1039.
- (13) Huang, J.; Wang, X.; Phuah, X.; Lu, P.; Qi, Z.; Wang, H. Plasmonic Cu Nanostructures in ZnO as Hyperbolic Metamaterial Thin Films. *Materials Today Nano* **2019**, *8*, 100052.
- (14) Zhang, D.; Lu, P.; Misra, S.; Wissel, A.; He, Z.; Qi, Z.; Gao, X.; Sun, X.; Liu, J.; Lu, J.; Zhang, X.; Wang, H. Design of 3D Oxide-Metal Hybrid Metamaterial for Tailorable Light-Matter Interactions in Visible and Near-Infrared Region. *Adv. Optical Mater.* **2021**, *9*, 2001154.
- (15) Huang, J.; Wang, X.; Li, D.; Jin, T.; Lu, P.; Zhang, D.; Lin, P.; Chen, H.; Narayan, J.; Zhang, X.; Wang, H. 3D Hybrid Plasmonic Framework with Au Nanopillars Embedded in Nitride Multilayers Integrated on Si. *Adv. Mater. Interfaces* **2020**, *7*, 2000493.
- (16) Hennes, M.; Fonda, E.; Casaretto, N.; Buchwald, J.; Weng, X.; Patriarche, G.; Demaille, D.; Zheng, Y.; Vidal, F. Structural, Vibrational, and Magnetic Properties of Self-assembled CoPt Nanoalloys Embedded in SrTiO<sub>3</sub>. *Phys. Rev. Materials* **2020**, 4, 126001.
- (17) Huang, J.; Phuah, X.; McClintock, L.; Padmanabhan, P.; Vikrant, K.; Wang, H.; Zhang, D.; Wang, H.; Lu, P.; Gao, X.; Sun, X.; Xu, X.; García, R.; Chen, H.; Zhang, X.; Wang, H. Core-shell Metallic Alloy Nanopillars-in-dielectric Hybrid Metamaterials with Magneto-plasmonic Coupling. *Mater. Today* **2021**, *51*, 39–47.
- (18) Song, J.; Zhang, D.; Lu, P.; Zhang, Y.; Wang, H.; Dou, H.; Xu, X.; Deitz, J.; Zhang, X.; Wang, H. Self-Assembled Complex Three-Phase Core-Shell Nanostructure of Au-CoFe<sub>2</sub>-TiN with a Magneto-Optical Coupling Effect. ACS Appl. Mater. Interfaces 2023, 15, 37810–37817.
- (19) Samardak, A.; Sukovatitsina, E.; Ognev, A.; Chebotkevich, L.; Mahmoodi, R.; Peighambari, S.; Hosseini, M.; Nasirpouri, F. Highdensity Nickel Nanowire Arrays for Data Storage Applications. *J. Phys. Conf. Ser.* **2012**, 345, 012011.
- (20) Citrin, D. Magnetic Bloch Oscillations in Nanowire Superlattice Rings. *Phys. Rev. Lett.* **2004**, 92, 196803.
- (21) Darques, M.; Spiegel, J.; de la Torre Medina, J.; Huynen, I.; Piraux, L. Ferromagnetic Nanowire-loaded Membranes for Microwave Electronics. J. Magn. Magn. Mater. 2009, 321, 2055–2065.

- (22) Nielsch, K.; Choi, J.; Schwirn, K.; Wehrspohn, R.; Gösele, U. Self-ordering Regimes of Porous Alumina: The 10 Porosity Rule. *Nano Lett.* **2002**, *2*, 677–680.
- (23) Huang, J.; Li, L.; Lu, P.; Qi, Z.; Sun, X.; Zhang, X.; Wang, H. Self-assembled Co-BaZrO<sub>3</sub> Nanocomposite Thin Films with Ultrafine Vertically Aligned Co Nanopillars. *Nanoscale* **2017**, *9*, 7970–7976
- (24) Zhang, B.; Huang, J.; Rutherford, B.; Lu, P.; Misra, S.; Kalaswad, M.; He, Z.; Gao, X.; Sun, X.; Li, L.; Wang, H. Tunable, Room-temperature Multiferroic Fe-BaTiO<sub>3</sub> Vertically Aligned Nanocomposites with Perpendicular Magnetic Anisotropy. *Materials Today Nano* 2020, 11, 100083.
- (25) Huang, J.; Qi, Z.; Li, L.; Wang, H.; Xue, S.; Zhang, B.; Zhang, X.; Wang, H. Self-assembled Vertically Aligned Ni Nanopillars in CeO<sub>2</sub> with Anisotropic Magnetic and Transport Properties for Energy Applications. *Nanoscale* **2018**, *10*, 17182–17188.
- (26) Osaka, T.; Takai, M.; Hayashi, K.; Ohashi, K.; Saito, M.; Yamada, K. A Soft Magnetic CoNiFe Film with High Saturation Magnetic Flux Density and Low Coercivity. *Nature* **1998**, 392, 796–798
- (27) Xiao, Y.; Xu, Q.; Zhang, J.; Yin, X.; Duan, S. Preparation and Magnetic Properties of Fe-Co-Ni Magnetic Nanowire Arrays with Three-Dimensional Periodic Structures. *J. Supercond. Nov. Magn.* **2023**, *36*, 1161–1170.
- (28) Samanifar, S.; Almasi Kashi, M.; Ramazani, A.; Alikhani, M. Reversal Modes in FeCoNi Nanowire Arrays: Correlation between Magneto-static Interactions and Nanowires Length. *J. Magn. Magn. Mater.* **2015**, *378*, 73–83.
- (29) Zheng, M.; Menon, L.; Zeng, H.; Liu, Y.; Bandyopadhyay, S.; Kirby, R. D.; Sellmyer, D. J. Magnetic Properties of Ni Nanowires in Self-assembled Arrays. *Phys. Rev. B* **2000**, *62*, 12282–12286.
- (30) Zeng, H.; Zheng, M.; Skomski, R.; Sellmyer, D. J.; Liu, Y.; Menon, L.; Bandyopadhyay, S. Magnetic Properties of Self-assembled Co Nanowires of Varying Length and Diameter. *J. Appl. Phys.* **2000**, 87, 4718–4720.
- (31) Han, G. C.; Zong, B. Y.; Luo, P.; Wu, Y. H. Angular Dependence of the Coercivity and Remanence of Ferromagnetic Nanowire Arrays. *J. Appl. Phys.* **2003**, *93*, 9202–9207.
- (32) Han, X. F.; Shamaila, S.; Sharif, R.; Chen, J. Y.; Liu, H. R.; Liu, D. P. Structural and Magnetic Properties of Various Ferromagnetic Nanotubes. *Adv. Mater.* **2009**, *21*, 4619–4624.
- (33) Javed, K.; Zhang, X. M.; Parajuli, S.; Ali, S. S.; Ahmad, N.; Shah, S. A.; Irfan, M.; Feng, J. F.; Han, X. F. Magnetization Behavior of NiMnGa Alloy Nanowires Prepared by DC Electrodeposition. *J. Magn. Magn. Mater.* **2020**, 498, 166232.
- (34) Ferrari, L.; Wu, C.; Lepage, D.; Zhang, X.; Liu, Z. Hyperbolic Metamaterials and Their Applications. *Progress in Quantum Electronics* **2015**, *40*, 1–40.
- (35) Lee, Y.; Kim, S.; Park, H.; Lee, B. Metamaterials and Metasurfaces for Sensor Applications. *Sensors* **2017**, *17*, 1726.
- (36) Liu, Y.; Bartal, G.; Zhang, X. All-angle Negative Refraction and Imaging in a Bulk Medium Made of Metallic Nanowires in the Visible Region. *Opt. Express* **2008**, *16*, 15439–15448.
- (37) Starko-Bowes, R.; Atkinson, J.; Newman, W.; Hu, H.; Kallos, T.; Palikaras, G.; Fedosejevs, R.; Pramanik, S.; Jacob, Z. Optical Characterization of Epsilon-near-zero, Epsilon-near-pole, and Hyperbolic Response in Nanowire Metamaterials. *J. Opt. Soc. Am. B* **2015**, 32, 2074–2080.
- (38) Novotny, L.; Hecht, B. *Principles of Nano-Optics*; Cambridge University Press, 2012.
- (39) Hoerman, B. H.; Ford, G. M.; Kaufmann, L. D.; Wessels, B. W. Dielectric Properties of Epitaxial Thin Films Dielectric Properties of Epitaxial BaTiO<sub>3</sub>Thin Films. *Appl. Phys. Lett.* **1998**, *73*, 2248–2250.
- (40) Gao, X.; Li, L.; Jian, J.; Wang, H.; Fan, M.; Huang, J.; Wang, X.; Wang, H. Vertically Aligned Nanocomposite BaTiO<sub>3</sub>:YMnO<sub>3</sub> Thin Films with Room Temperature Multiferroic Properties toward Nanoscale Memory Devices. *ACS Appl. Nano Mater.* **2018**, *1*, 2509–2514.

- (41) Lorenz, M.; Hirsch, D.; Patzig, C.; Höche, T.; Hohenberger, S.; Hochmuth, H.; Lazenka, V.; Temst, K.; Grundmann, M. Correlation of Interface Impurities and Chemical Gradients with High Magnetoelectric Coupling Strength in Multiferroic BiFeO<sub>3</sub>-BaTiO<sub>3</sub> Superlattices. *ACS Appl. Mater. Interfaces* **2017**, *9*, 18956–18965.
- (42) Revathy, R.; Kalarikkal, N.; Varma, M.; Surendran, K. Exotic Magnetic Properties and Enhanced Magnetoelectric Coupling in Fe<sub>3</sub>O<sub>4</sub>-BaTiO<sub>3</sub> Heterostructures. *J. Alloys Compd.* **2021**, 889, 161667. (43) Huang, J.; Jin, T.; Misra, S.; Wang, H.; Qi, Z.; Dai, Y.; Sun, X.; Li, L.; Okkema, J.; Chen, H.; Lin, P.; Zhang, X.; Wang, H. Tailorable Optical Response of Au-LiNbO<sub>3</sub> Hybrid Metamaterial Thin Films for Optical Waveguide Applications. *Adv. Optical Mater.* **2018**, 6, 1800510.
- (44) Huang, J.; Wang, H.; Li, D.; Qi, Z.; Zhang, D.; Lu, P.; Chen, H.; Yarotski, D.; Lin, P.; Zhang, X.; Wang, H. Room-Temperature Ferroelectric LiNb $_6$ Ba $_5$ Ti $_4$ O $_{30}$  Spinel Phase in a Nanocomposite Thin Film Form for Nonlinear Photonics. *ACS Appl. Mater. Interfaces* **2020**, 12, 23076–23083.